RSC Advances

PAPER

View Article Online
View Journal | View Issue

Cite this: *RSC Adv.*, 2017, **7**, 44499

Half-metals and half-semiconductors in a transition metal doped $SnSe_2$ monolayer: a first-principles study

Xuming Wu,[a] Jiangchao Han,[a] Yulin Feng,[a] Guanpeng Li,[a] Cong Wang,[a] Guangqian Ding[b] and Guoying Gao *[a]

Recently, a new two-dimensional (2D) semiconductor $SnSe_2$ monolayer has been grown by molecular beam epitaxy, and weak ferromagnetic behavior above room temperature in Mn-doped $SnSe_2$ thin films was also observed experimentally. Here, using first-principles calculations, we investigate the structural, electronic, and magnetic properties of an $SnSe_2$ monolayer doped with transition metals V, Cr, Mn, Fe, Co, Ni and Cu. The calculated formation energies indicate that it is energetically favorable and relatively easy to incorporate these transition metals except for Cu into the $SnSe_2$ monolayer under Se-rich conditions. Doping induces considerable magnetic moments except for the Ni-doped system. Long-range ferromagnetic order is observed for V, Cr and Fe doping, and Mn doping has a short-range ferromagnetic order. Cu doping has an antiferromagnetic ground state. Within generalized gradient approximation, interestingly, both ferromagnetic V doping and metastable ferromagnetic Cu doping exhibit half-metallicity. Both Mn- and Fe-doped $SnSe_2$ monolayers are half-semiconductors. These properties are governed by the transition metal 3d orbital splitting under the crystal field and p–d hybridization. Within hybrid functional or spin–orbit coupling, the V-doped $SnSe_2$ monolayer becomes a half-semiconductor, and the Cu-doped $SnSe_2$ monolayer is still a half-metal. These studies indicate the promising spintronic applications for 2D semiconductor $SnSe_2$ doped by transition metals.

Received 12th July 2017
Accepted 11th September 2017

DOI: 10.1039/c7ra07648g

rsc.li/rsc-advances

1. Introduction

In recent years, half-metallic magnets (HMMs)[1] have attracted considerable research interest in spintronic applications, because their band structure is metallic in only one of the two spin channels (Fig. 1(a)), leading to 100% spin polarization of electrons around the Fermi level. So, HMMs have been seen as the most promising candidates for spin-injector materials, and they are the key materials used to fabricate spintronic devices such as spin valves, spin field effect transistors, and spin filters.[2] Several classes of HMMs have been fabricated experimentally or predicted theoretically, *e.g.*, Heusler alloys, metallic oxides, transition-metal pnictides and chalcogenides, *etc.*[3–5] In addition to HMMs, half-semiconductors (HSCs)[6] are also a class of spintronic materials with 100% spin polarization, because their conduction band and valence band are spin split with the conduction band minimum and valence band maximum possessing the same spin channel (Fig. 1(b)).

Previous studies on HMMs and HSCs mainly focused on the bulk systems. Searching for HMMs and HSCs in graphene-like two-dimensional (2D) materials is interesting due to the advantages of ultrathin thickness (monolayer or few atomic layers), extraordinary electronic properties and facile synthesis. However, most of pristine graphene-like 2D materials have been found to be nonmagnetic, and several ones were predicted to be HMMs and HSCs.[7–10] The emergence of magnetism in 2D materials usually needs external electric field, edge-functionalizing, vacancy, defect, strain and doping.[8,11,12] Experimentally, substitutional doping has been proved to be

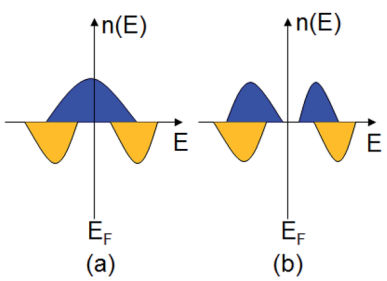

Fig. 1 The schemes of density of states $n(E)$ as a function of energy E for (a) a half-metal and (b) a half-semiconductor. Blue and yellow present the spin-up and spin-down states, respectively.

[a]*School of Physics and Wuhan National High Magnetic Field Center, Huazhong University of Science and Technology, Wuhan 430074, China. E-mail: guoying_gao@mail.hust.edu.cn*

[b]*School of Science, Chongqing University of Posts and Telecommunications, Chongqing, 400065, China*

a powerful route to induce ferromagnetism in some 2D materials such as Co and Cu-doped MoS_2.[13,14] Few HMMs and HSCs have been predicted in some MoS_2-like 2D materials doped by transition metal (TM) atoms.[15–17]

Very recently, a new 2D semiconductor of $SnSe_2$ monolayer has been grown by molecular beam epitaxy,[18] and few-layer $SnSe_2$ field effect transistor with a high current on/off ratio of 10^4 was also fabricated successfully.[19] The studies on 2D $SnSe_2$ mainly focused on the electronic and optoelectronic properties. Interestingly, a recent experiment revealed weak ferromagnetic behavior above room temperature in Mn-doped $SnSe_2$ thin films, and importantly, even rather large concentrations of Mn (up to 0.6) do not destroy the 2D crystal structure of the parent $SnSe_2$,[20] which motivates us to search for HMMs and HSCs in 2D $SnSe_2$ doped by Mn and other TM atoms. In this paper, we use the first-principles calculations to systemically investigate the electronic and magnetic properties of TM-doped $SnSe_2$ monolayer (TM = V, Cr, Mn, Fe, Co, Ni, Cu). It is found that the structures of the doped systems except for Cu doping are energetically stable. Within generalized gradient approximation, both V- and Cu-doped $SnSe_2$ monolayers exhibit half-metallicity, and both Mn- and Fe-doped $SnSe_2$ monolayers are HSCs. Within hybrid functional or spin–orbit coupling, V-doped $SnSe_2$ monolayer becomes a half-semiconductor, and Cu-doped $SnSe_2$ monolayer is still a half-metal. These results indicate that TM-doped $SnSe_2$ monolayers are promising candidates for 2D spintronic applications.

2. Computational details

The present work is performed by using the first-principles full-potential linearized augmented plane-wave method (Wien2k package)[21] within the generalized gradient approximation (GGA) with the Perdew–Burke–Ernzerhof (PBE) scheme[22] for the electronic exchange–correlation functional. We also consider the effects of hybrid functional and spin–orbit coupling on the electronic structures. The relativistic effect in the scalar approximation is considered. The radii R_{mt} of the muffin tins are chosen to be approximately proportional to the corresponding ionic radii and as large as possible under the condition that the spheres do not overlap. The $R_{mt}K_{max}$ relating to the energy cutoff is taken as 8.5. We adopt the $12 \times 12 \times 1$ k meshes in the Brillouin zone integration. The self-consistency calculations are considered to be achieved when the total energy difference between succeeding iterations is less than 10^{-5} Ry per formula unit.

$SnSe_2$ bulk has the layered CdI_2-type (T-type) structure with the space group of $P\bar{3}m1$ and the in-plane lattice constant of 3.81 Å.[23] For the structural model of TM-doped $SnSe_2$ monolayer, we adopt the $4 \times 4 \times 1$ supercell of $SnSe_2$ monolayer with a 15 Å vacuum, and one Sn atom is replaced by one TM atom for the calculations of formation energy, band structure and density of states, which is shown in Fig. 2. So, the doping concentration is 6.25%. For the calculations of magnetic order stability, we replace two Sn atoms by two TM atoms. The lattice constant of $SnSe_2$ monolayer is based on our optimized value of 3.86 Å.[24] Before calculating the electronic and magnetic properties, we perform the structural relaxation of TM-doped $SnSe_2$ monolayer, and the optimized bond lengths of TM–Se atoms are collected in Table 1.

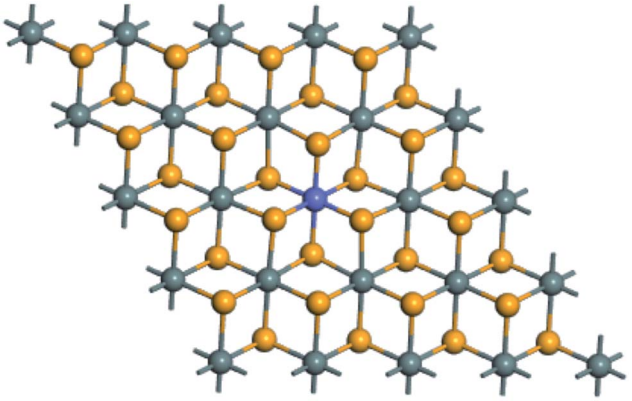

Fig. 2 Top view of $SnSe_2$ monolayer doped by one TM atom based on the $4 \times 4 \times 1$ supercell. The grayish, yellow and blue balls represent Sn, Se and TM atoms, respectively.

Table 1 The calculated bond length d_{TM-Se} (in Å) between TM (transition metal) and nearest neighboring Se atoms, total magnetic moment M_{tot} (in μ_B), formation energies E_{for} (in eV) under Sn rich and Se rich, total energy difference between antiferromagnetic (AFM) and ferromagnetic (FM) states ΔE_i (in meV), and estimated Curie temperatures T_C (in K) for the $4 \times 4 \times 1$ supercell of $SnSe_2$ monolayer doped by TM atoms. Note that the subscripts 1, 2 and 3 in ΔE_i correspond to the three cases of nearest neighboring, next-nearest neighboring and third-nearest neighboring of two TM atoms, respectively

Doping	d_{TM-Se}	M_{tot}	$E_{for(Sn\text{-}rich)}$	$E_{for(Se\text{-}rich)}$	ΔE_1	ΔE_2	ΔE_3	T_C
V	2.546	1.00	−0.19	−1.30	50	34	21	193
Cr	2.618	2.55	−0.12	−1.23	121	31	24	468
Mn	2.733	3.00	0.55	−0.56	37	3	1	143
Fe	2.458	2.00	0.88	−0.22	76	26	18	294
Co	2.424	0.83	0.94	−0.17	59	14	2	228
Ni	2.457	0	0.71	−0.40	0	0	0	—
Cu	2.539	1.00	2.27	1.15	−53	−4	−2	—

3. Results and discussion

3.1. Structural stability and magnetic stability

As mentioned above, Mn-doped $SnSe_2$ thin films has been fabricated experimentally,[20] and thus it is necessary to explore and compare the structural stability of $SnSe_2$ monolayer doped by different TM atoms. We calculate the formation energy by[15,25]

$$\Delta E_f = E_{(doped)} - E_{(pristine)} - n\mu_{TM} + n\mu_{Sn}, \quad (1)$$

where $E_{(doped)}$ and $E_{(pristine)}$ are the total energies of the $4 \times 4 \times 1$ supercell of $SnSe_2$ monolayer with and without TM dopants, respectively, and n is the number of Sn atoms replaced by TM atoms. One Sn atom is replaced by one TM atom, and thus n is 1. μ_{Sn} and μ_{TM} are the chemical potentials of Sn and TM atoms, which depend on the experimental growth conditions and satisfy the boundary conditions. The total energy per TM atom

in bulk TM is adopted for μ_{TM}. For a Sn-rich condition, μ_{Sn} is taken as the total energy per Sn atom in bulk Sn, while for a Se-rich condition, μ_{Sn} is the total energy difference between two Se atoms and one formula unit of stoichiometric $SnSe_2$ monolayer. Table 1 lists the calculated formation energies of TM-doped $SnSe_2$ monolayer in Sn rich and Se rich conditions. One can see that the formation energies under the same Sn(Se)-rich condition for all TM-doped systems except for Cu doping are comparable, and the formation energies under Se-rich condition are negative and lower than those under Sn-rich condition, which indicates that, like the experimental Mn-doped $SnSe_2$,[20] it is energetically favorable and relatively easier to incorporate V, Cr, Fe, Co and Ni atoms into $SnSe_2$ monolayer under the Se-rich experimental condition, which is similar to that of Zn-doped SnS_2 monolayer.[25] It may be not easy to realize the Cu-doped $SnSe_2$ monolayer due to the positive formation energy under Sn-rich or Se-rich condition.

Stable ferromagnetism of a material is crucial for the spintronic applications, and thus we study the magnetic stability of TM-doped $SnSe_2$ monolayer. We need compare the ferromagnetic (FM) and antiferromagnetic (AFM) interactions, and thus two Sn atoms are replaced by two same TM atoms in the $4 \times 4 \times 1$ supercell of $SnSe_2$ monolayer. The FM and AFM configurations are set by the parallel and antiparallel spin orientations between the two TM atoms, respectively. Usually, magnetic interactions between two TM dopants will change with the change of TM–TM distance. Here, we consider two nearest neighboring, next-nearest neighboring and third-nearest neighboring TM atoms. Table 1 lists the calculated total energy difference between the AFM and FM states. It shows that the Ni-doped system is nonmagnetic independent of the Ni–Ni distance. The Cu-doped system has a short-range AFM ground state. All the V-, Cr-, Mn, Fe- and Co-doped systems have lower FM total energies than the AFM states. The FM order is long-range for all the V, Cr and Fe dopants, but it is short-range for the Mn dopants. We also note that the total energy differences between AFM and FM states under nearest neighboring sites are considerable (from 37 to 121 meV per supercell), which mean these V-, Cr-, Mn-, Fe- and Co-doped systems should have high-temperature ferromagnetism. In fact, FM behavior above room temperature has been realized in the recent experiment of Mn-doped $SnSe_2$ thin films.[20]

3.2. Electronic structure and magnetism

In order to search for possible half-metals and HSCs, we show in Fig. 3(a)–(g) the calculated spin-resolved band structure of $SnSe_2$ monolayer doped by one TM atom within GGA–PBE. For comparison, the electronic band structure of pristine $SnSe_2$ monolayer is also presented. As shown in Fig. 1(h), pristine $SnSe_2$ monolayer is a nonmagnetic semiconductor, and the calculated indirect gap ($\Gamma - M$) of 0.85 eV is in agreement with the previous value of 0.80 eV.[26] The indirect gap of $SnSe_2$ monolayer is larger than that of $SnSe_2$ bulk (0.71 eV).[27] The valence bands around the Fermi level are mainly composed of hybridized Se p electrons with Sn p electrons, and the conduction bands around the Fermi level mainly originate from the hybridized Sn s electrons with Se p electrons. For the doped systems, both V- and Cu-doped $SnSe_2$ monolayers exhibit a HM characteristic, because the spin-up electrons cross the Fermi level, indicating metallicity, while the spin-down band structure is semiconducting. Ni-doped $SnSe_2$ monolayer is a nonmagnetic semiconductor, and both Cr- and Co-doped $SnSe_2$ monolayers are usual magnetic semiconductors. Interestingly, both Mn- and Fe-doped $SnSe_2$ monolayers are HSCs, because both conduction band and valence band are spin split, and the conduction band minimum and valence band maximum possess the same spin down channel. We note that the calculated integer magnetic moments shown in Table 1 also reflect the characteristics of half-metals for both V- and Cu-doped $SnSe_2$ monolayers and HSCs for both Mn- and Fe-doped $SnSe_2$ monolayers. The magnetic moments are mainly from the TM atoms and the nearest neighboring Se atoms.

Here, we mainly focus on the doped systems with complete spin polarization, *i.e.*, the half-metals of V- and Cu-doped $SnSe_2$ monolayer and the HSCs of Mn- and Fe-doped $SnSe_2$ monolayer. In order to better understand the electronic structure and magnetism, we present in Fig. 4 the calculated total and main partial density of states (DOS) within GGA–PBE for $SnSe_2$ monolayer doped with V and Mn as the examples of half-metals and HSCs, respectively. The total DOSs around the Fermi level are mainly from the TM 3d electrons and the nearest neighboring Se 4p electrons. One can see from Fig. 4 that there is a large exchange splitting for 3d electrons of V and Mn, providing the main spin magnetic moments in the doped systems. There are obvious orbital hybridization between TM 3d electrons and Se 4p electrons, which induces small magnetic moment in nearest neighboring Se atoms. Under the crystal field of CdI_2-type structure, the V (Mn) 3d orbitals are split into a single a (d_{z^2}), twofold degenerate e_1 (d_{xy}, $d_{x^2-y^2}$) and twofold degenerate e_2 (d_{xz}, d_{yz}) states. For the case of V-doped system, one know from Fig. 4(a) and 3(a) that one 3d electron in V^{4+} ($3d^1$) occupies partially the spin-up twofold degenerate e_1 states, exhibiting metallicity, while the spin-down 3d states are almost empty, showing semiconductivity, and thus the V-doped system is a HM ferromagnet with the net spin magnetic moment of one μ_B. The twofold degenerate e_2 states mainly take part in the orbital hybridization between V 3d electrons and Se 4p electrons. Similarly, for the case of Mn-doped system, as shown in Fig. 4(b), both spin-up and spin-down electrons show a semiconductor characteristic, because three 3d electrons in Mn^{4+} ($3d^3$) occupy fully the spin-up twofold degenerate e_1 states and the spin-up single a state, and the spin-down 3d states are almost empty. The large exchange split of e_2 states makes the energy of the bottom of spin-up e_2 states is higher than that of the top of spin-down e_1 states, inducing the characteristic of a HSC in Mn-doped $SnSe_2$ monolayer. In addition, only the Ni-doped $SnSe_2$ monolayer is a nonmagnetic semiconductor in all the doped systems studied, which is not difficult to understand, because both spin-up and spin-down twofold degenerate e_1 states and single a state are fully occupied by six 3d electrons in Ni^{4+} ($3d^6$), inducing zero magnetic moment.

Using the relation $K_B T_C = \frac{2}{3}\frac{\Delta E}{n_{imp}}$ based on the classical Heisenberg model and the mean-field approximation (MFA),[28] we estimate the Curie temperature T_C, where ΔE is the total

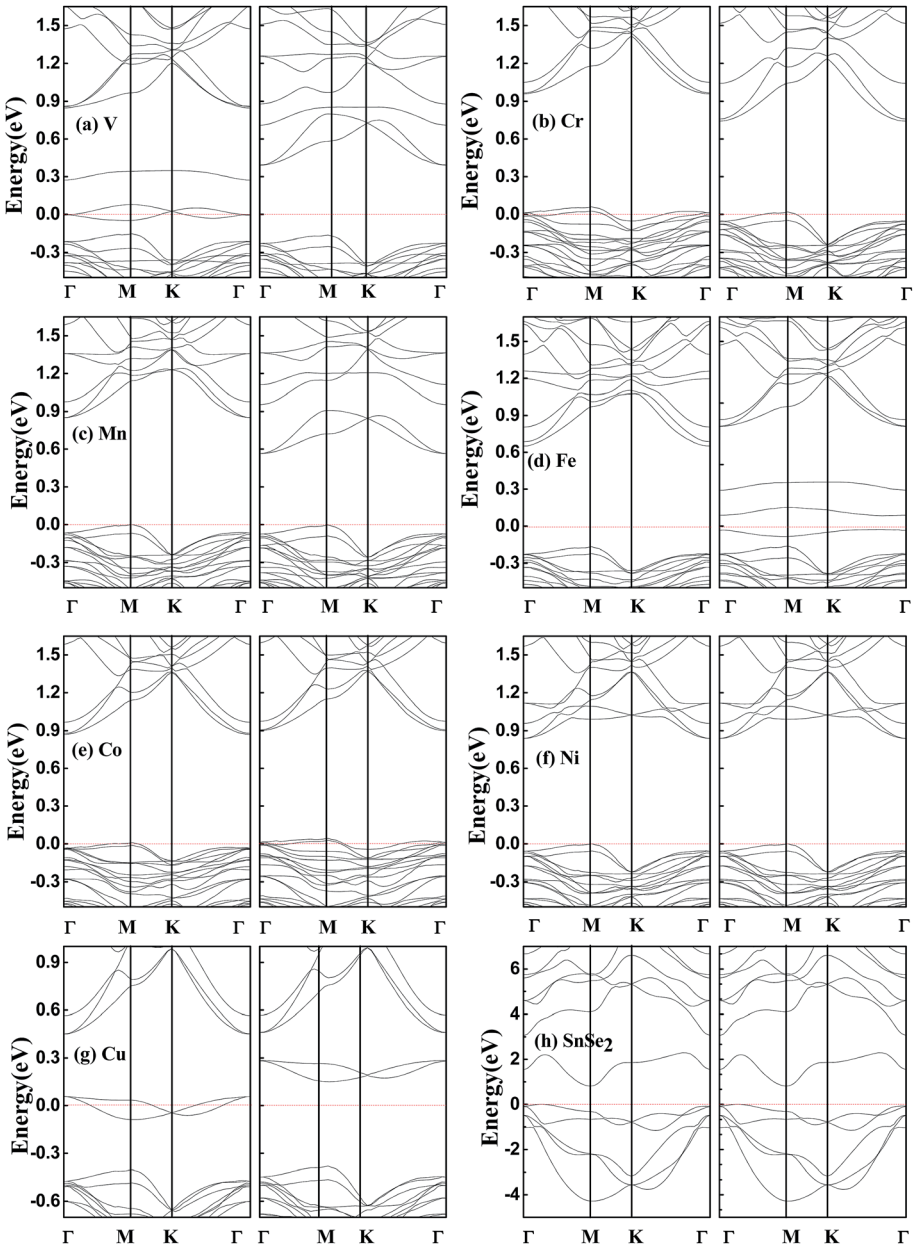

Fig. 3 Calculated spin-resolved band structures within GGA–PBE. (a–g) $SnSe_2$ monolayer doped by one V, Cr, Mn, Fe, Co, Ni and Cu atom, respectively. (h) Pristine $SnSe_2$ monolayer. The red dashed line represents the Fermi level at zero eV.

energy difference between AFM and FM states under nearest neighboring sites for the $4 \times 4 \times 1$ supercell of doped $SnSe_2$ monolayer (see Table 1), and n_{imp} is the number of TM atoms in the supercell. This method has been extensively used to estimate the Curie temperatures for some TM-doped 2D semiconductors such as phosphorene, germanane, and MoS_2.[29–31] The estimated Curie temperatures are listed in Table 1. One can see that the values are high especially for the Cr- and Fe-doped systems, which makes them promising candidates for 2D spintronic applications. We note that our estimated Curie temperatures of doped $SnSe_2$ monolayers are higher than those of doped MoS_2 monolayers.[31] In addition, the estimated Curie temperature of Mn-doped $SnSe_2$ monolayer is lower than the experimental value (above room temperature).[20] The reason may be the different Mn doping concentration and the different thickness of $SnSe_2$ thin films. The Mn doping concentration in experiment is much higher than that in our present theory, and the experimental doped $SnSe_2$ thin films is thicker than the doped $SnSe_2$ monolayer we studied. So, it is meaningful to explore the Curie temperatures dependent of the doping concentration and the thickness of $SnSe_2$ films in future works.

Finally, it should be pointed out that above band structures are based on the GGA–PBE for the electronic exchange–correlation functional, and band structures may be different within different functionals. Hybrid functional HSE can usually increase the energy gap of a semiconductor compared to GGA,

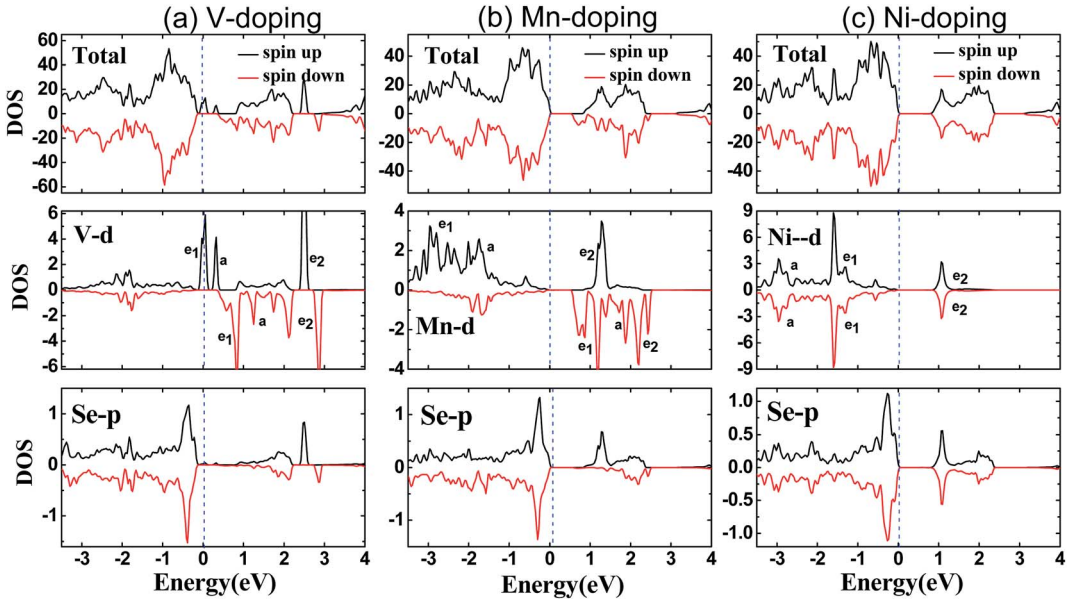

Fig. 4 Calculated spin-resolved total and main partial density of states of 3d states of TM atoms and 4p states of nearest neighboring Se atoms in $SnSe_2$ monolayer doped by one V (a), Mn (b), and Ni (c) atom within GGA–PBE. The dashed line represents the Fermi level at zero eV.

but the semiconductor property can not be destroyed.[24] Considering that all the doped systems studied are semiconductors except for V- and Cu-doped $SnSe_2$ monolayers which are half-metals within GGA-PBE, we perform spin-resolved band structure calculations for V- and Cu-doped $SnSe_2$ monolayers within HSE. As shown in Fig. 5, Cu-doped $SnSe_2$ monolayer is still a half-metal. Although V-doped $SnSe_2$ monolayer is not a half-metal, it becomes a HSC, and the spin polarization is still complete. Comparing Fig. 5(a) with Fig. 3(a), it is clear that, for both spin-up and spin-down channels of V-doped $SnSe_2$ monolayer, the valence bands within HSE move toward the Fermi level compared to those within GGA–PBE, while the conduction bands shift to high energy range (depart from the Fermi level). The spin split becomes weak within HSE compared to GGA–PBE. In addition, we check the effect of spin–orbit coupling (SOC) on the band structures of V- and Cu-doped $SnSe_2$ monolayers. The calculated band structures within SOC shown in Fig. 6 indicate that V-doped $SnSe_2$ monolayer is no longer a half-metal, and it is a HSC with a very small energy gap

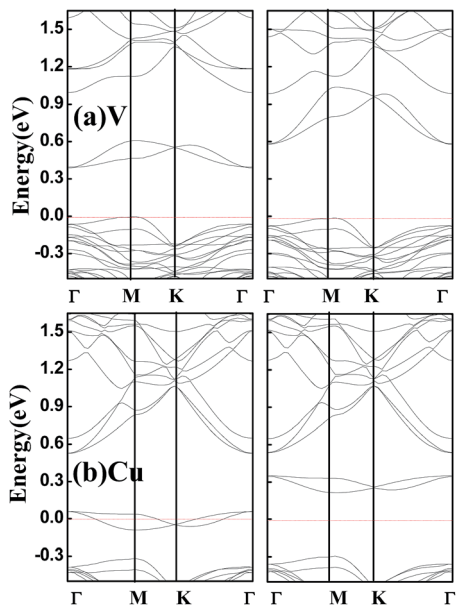

Fig. 5 Calculated spin-resolved band structures within HSE for $SnSe_2$ monolayer doped by V (a) and Cu (b). The red dashed line represents the Fermi level at zero eV.

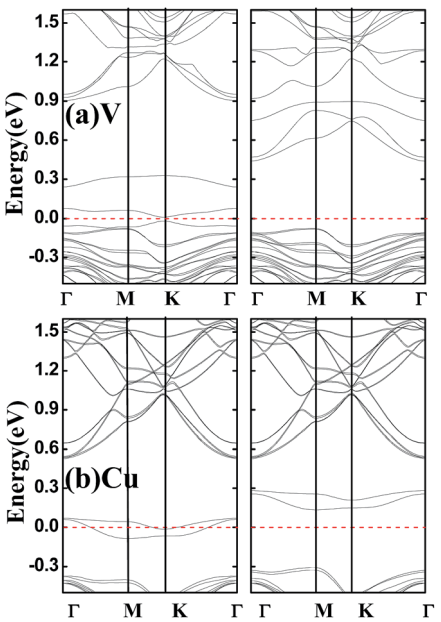

Fig. 6 Calculated spin-resolved band structures within GGA–PBE and SOC for $SnSe_2$ monolayer doped by V (a) and Cu (b). The red dashed line represents the Fermi level at zero eV.

in the spin-up channel. Half-metallicity is still observed in Cu-doped $SnSe_2$ monolayer. So, no matter GGA, HSE or SOC, both V- and Cu-doped $SnSe_2$ monolayers are high spin-polarized materials.

4. Conclusions

We have used the first-principles full-potential linearized augmented plane-wave method to explore the structural, electronic and magnetic properties of V-, Cr-, Mn-, Fe-, Co-, Ni- and Cu-doped $SnSe_2$ monolayer. We show from the calculated formation energy that it is easier for substituted doping of $SnSe_2$ monolayer under Se-rich condition except for Cu doping. All the V-, Cr-, Mn-, Fe-, and Co-doped systems have a ferromagnetic ground state, and the Cu-doped system is most stable in antiferromagnetic state, while the Ni-doped system is nonmagnetic. Ferromagnetic orders of V, Cr and Fe dopants are long-range, but it is short-range for ferromagnetic Mn dopants and for antiferromagnetic Cu dopants. Within GGA–PBE, we predict the HM ferromagnetism in V-doped $SnSe_2$ monolayer with 1.00 μ_B per supercell, and metastable ferromagnetic Cu-doped $SnSe_2$ monolayer also exhibits half-metallicity. Half-semiconductors are found in doping of Mn and Fe with the magnetic moments of 3.00 and 2.00 μ_B per supercell, respectively. Within HSE or SOC, Cu-doped $SnSe_2$ monolayer is still a half-metal, while V-doped $SnSe_2$ monolayer becomes a HSC. Based on the classical Heisenberg model and the mean-field approximation, the estimated curie temperatures of TM-doped $SnSe_2$ monolayers are high, which make them promising candidates for 2D spintronic applications.

Conflicts of interest

There are no conflicts to declare.

Acknowledgements

This work was supported by the National Natural Science Foundation of China under Grant No. 11474113, by the Natural Science Foundation of Hubei Province under Grant No. 2015CFB419, and by the Fundamental Research Funds for the Central Universities under Grant No. HUST: 2015TS019.

References

1 R. A. de Groot, F. M. Mueller, P. G. van Engen and K. H. J. Buschow, *Phys. Rev. Lett.*, 1983, **50**, 2024–2027.
2 I. Zutic, J. Fabian and S. S. Sarma, *Rev. Mod. Phys.*, 2004, **76**, 323–410.
3 C. Felser, G. H. Fecher and B. Balke, *Angew. Chem., Int. Ed.*, 2007, **46**, 668–699.
4 S. Skaftouros, K. Ozdogan, E. Sasiogl and I. Galanakis, *Phys. Rev. B: Condens. Matter Mater. Phys.*, 2013, **87**, 024420.
5 X. Wang, Z. Cheng, J. Wang, L. Wang, Z. Yu, C. Fang, J. Yang and G. Liu, *RSC Adv.*, 2016, **6**, 57041–57047.
6 X. Li and J. Yang, *Natl. Sci. Rev.*, 2016, **3**, 365–381.
7 E. Torun, H. Sahin, S. K. Singh and F. M. Peeters, *Appl. Phys. Lett.*, 2015, **106**, 192404.
8 G. Gao, G. Ding, J. Li, K. Yao, M. Wu and M. Qian, *Nanoscale*, 2016, **8**, 8986–8994.
9 M. Mushtag, Y. Zhou and X. Xiang, *RSC Adv.*, 2017, **7**, 22541–22547.
10 W. Zhang, Q. Qu, P. Zhu and C. Lam, *J. Mater. Chem. C*, 2015, **3**, 12457–12468.
11 Z.-K. Tang, W.-W. Liu, D.-Y. Zhang, W.-M. Lau and L.-M. Liu, *RSC Adv.*, 2015, **5**, 77154–77158.
12 I. Khan and J. Hong, *Nanotechnology*, 2016, **27**, 385701.
13 Z. Xiang, Z. Zhang, X. Xu, Q. Zhang, Q. Wang and C. Yuan, *Phys. Chem. Chem. Phys.*, 2015, **17**, 15822–15828.
14 B. Xia, Q. Guo, D. Gao, S. Shi and K. Tao, *J. Phys. D: Appl. Phys.*, 2016, **49**, 165003.
15 X. Zhao, T. Wang, S. Wei, X. Dai and L. Yang, *J. Alloys Compd.*, 2017, **695**, 2048–2053.
16 T. Wang, Y. Li, C. Xia, X. Zhao, Y. An and X. Dai, *J. Mater. Chem. C*, 2016, **4**, 8111–8120.
17 J. Thakur, M. K. Kashyap, H. S. Saini and A. H. Reshak, *J. Alloys Compd.*, 2015, **649**, 1300–1305.
18 Y. W. Park, *et al.*, *2D Mater.*, 2017, **4**, 014006.
19 T. Pei, L. Bao, G. Wang, R. Ma, H. Yang, J. Li, C. Gu, S. Pantelides, S. Du and H.-J. Gao, *Appl. Phys. Lett.*, 2016, **108**, 053506.
20 S. Dong, *et al.*, *APL Mater.*, 2016, **4**, 032601.
21 P. Blaha, K. Schwarz, G. K. H. Madsen, D. Kvasnicka and J. Luitz, *Wien2k*, improved and updated Unix version of the original copyrighted Wien code, which was published by, Vienna University of Technology, 2002; P. Blaha, K. Schwarz, P. Sorantin and S. B. Trickey, *Comput. Phys. Commun.*, 1990, **59**, 399.
22 J. P. Perdew, K. Burke and M. Ernzerhof, *Phys. Rev. Lett.*, 1996, **77**, 3865.
23 H. Liu and L. L. Y. Chang, *J. Alloys Compd.*, 1992, **185**, 183–190.
24 G. Li, G. Ding and G. Gao, *J. Phys.: Condens. Matter*, 2017, **29**, 015001.
25 L. Sun, W. Zhou, Y. Liu, D. Yu, Y. Liang and P. Wu, *Appl. Surf. Sci.*, 2016, **389**, 484–490.
26 S. Lebegue, T. Björkman, M. Klintenberg, R. M. Nieminen and O. Eriksson, *Phys. Rev. X*, 2013, **3**, 031002.
27 B. Sun, Z. Ma, C. He and K. Wu, *Phys. Chem. Chem. Phys.*, 2015, **17**, 29844–29853.
28 J. Kudrnovsky, I. Turek, V. Drchal, F. Maca, P. Weinberger and P. Bruno, *Phys. Rev. B: Condens. Matter*, 2004, **69**, 115208.
29 L. Seixas, A. Carvalho and A. H. C. Neto, *Phys. Rev. B: Condens. Matter*, 2015, **91**, 155138.
30 M. Sun, Q. Ren, Y. Zhao, S. Wang, J. Yu and W. Tang, *J. Appl. Phys.*, 2016, **119**, 143904.
31 Y. Cheng, Z. Zhu, W. Mi, Z. Guo and U. Schwingenschlogl, *Phys. Rev. B: Condens. Matter Mater. Phys.*, 2013, **87**, 100401(R).

